PAPER

Check for updates

Tuning the arrangement of atoms in SAPO-34 molecular sieves for a deeper understanding of their performance in the MTO reaction

Ludovica Pace, [iD][a] Junwei Wu, [iD][a] Marco G. Geloso, [iD][a] Francesco Dalena, [iD][a] Diogenes Honorato-Piva, [iD][a] Eddy Dib [iD]*[b] and Svetlana Mintova [iD]*[a]

The catalytic properties of SAPO-34 molecular sieves synthesized using two different organic structure-directing agents (OSDAs), triethylamine (TEA) and tetraethylammonium (TEA$^+$), were investigated in the methanol-to-olefin (MTO) reaction. Although both OSDAs lead to the same CHA-type structure, the two samples exhibit distinct physicochemical properties inducing different performances in the MTO reaction. The amount of incorporated silicon is higher in the SAPO-34 synthesized with TEA (sample N-C), while a higher concentration of Si(4Al) species is obtained when TEA$^+$ (sample P-C) is used. Additionally, the size of the crystals decreased significantly when using TEA$^+$. The differences observed in activity are mainly due to different textural properties and silicon distribution; TEA$^+$ favours the formation of nanocrystals where the dispersion of Si gives rise to a high concentration of Brønsted acidic sites while TEA favours the clustering of Si in 'islands' in micron-sized crystals, influencing the catalytic performance of SAPO-34 in the MTO reaction. The N-C sample exhibits high initial selectivity toward light olefins (C$_2$–C$_4$) and strong hydrogen transfer activity, but undergoes rapid deactivation due to its larger crystal size that promotes coke formation. In contrast, the P-C sample shows slightly lower initial selectivity but superior stability and lifetime, enabled by its nanoscale crystal size, larger external surface area, and higher acid site density, which together enhance diffusion, limit coke deposition, and sustain methanol conversion.

Introduction

Since zeolites are defined as crystalline porous aluminosilicates, the term zeotypes or zeolitic materials appear to refer to similar porous materials with different chemical compositions. The term was first used to describe aluminophosphates (AlPO$_4$) and silicoaluminophosphates (SAPO) where silicon atoms substitute some of the tetrahedral aluminium and phosphorus atoms in the structures.[1,2] Although many other structures are now considered as zeotypes such as gallosilicates,[3] gallophosphates,[4] gallogermanates,[5] borosilicates[6] and zincophosphates,[7] AlPOs are the most investigated and the International Zeolite Association (IZA) recognizes more than 50 frameworks to date.[8] AlPO materials are electrically neutral because their frameworks contain alternating [AlO$_4$]$^-$ and [PO$_4$]$^+$ tetrahedra. When [SiO$_4$] units are incorporated, this charge balance is disrupted, creating negatively charged sites that must be compensated by extra-framework cations (*e.g.*, protons), thereby generating Brønsted acid sites.[9] The numbering of structure types of SAPO-*n* follows the one used for AlPO$_4$-*n*, for example, SAPO-5 denotes the same structure type as AlPO$_4$-5. SAPOs are closely related to their AlPOs; however, some of the phosphorus or/and aluminium atoms are replaced by silicon atoms generating mild acidity compared to zeolites.[10] In addition to weak acid sites originating from the surface (P–OH, Si–OH or Al–OH groups), the acid sites appear in the form of bridging hydroxyl groups as in zeolites.[11] Note that the maximum concentration of Brønsted acid sites in SAPO materials cannot exceed the Si content. Two substitution mechanisms (SMs) have been proposed for the incorporation of Si into the AlPO frameworks. SM$_2$ involves the substitution of phosphorus with silicon and hydrogen (P → Si, H), with the proton being linked to an oxygen atom on a Si–O–Al bridge, forming a bridging hydroxyl group –Si(OH)Al– that acts as a Brønsted acid site.[12] The second mechanism (SM$_3$) encompasses the double substitution of adjacent aluminium and phosphorus atoms with two silicon atoms (Al, P → Si, Si), resulting in a lower concentration of new acid sites. This leads to the formation of Si islands where Si may be surrounded by up to 4 Si atoms

[a] *Université de Caen Normandie, ENSICAEN, CNRS, LCS, Laboratoire Catalyse et Spectrochimie, 14000 Caen, France. E-mail: svetlana.mintova@ensicaen.fr*
[b] *CEMHTI, CNRS, University of Orléans, 1D avenue de la Recherche Scientifique, 45071, Orléans, France. E-mail: eddy.dib@ensicaen.fr*

linked by oxygen bridges then giving rise to less Brønsted acid sites.[13] In addition, the incorporation of silicon atoms may result from the combination of both mechanisms: SM_2 + SM_3.[14]

Consequently, the silicoaluminophosphate framework can be represented as a combination of two main parts: aluminosilicate areas (SA), in which silicon atoms are concentrated with the possible presence of some aluminium atoms, and silicoaluminophosphate (SAPO) areas, in which silicon atoms are well dispersed in the aluminophosphate matrix.[15] Due to the occurrence of such substitution mechanisms, BASs cover a wide range of acidity in SAPOs arising from the formation of Si(n Al, $(4 − n)$ Si) $(0 < n < 4)$ species. Thus, the acidic features of SAPOs are highly dependent on the nature of the Si species and their distribution. Establishing a direct correlation between the quantity of acid sites and the Si content is a complex task due to the involvement of different mechanisms for the incorporation of Si into the SAPO framework.[16] Thus, the amount of these acid sites depends on the dimension of the concerned island, intimately related to the Si concentration,[17] with both the concentration and the strength of acid sites being determined by the Si substitution mechanisms.

SAPOs with controllable acidic characters are widely used in various catalytic processes such as hydro-isomerization,[18] methanol-to-olefin reactions[19,20] and ammonia selective catalytic reduction.[21,22] SAPO-34 (CHA topology) is an important member in the family of SAPOs, it is known as an excellent catalyst for the selective formation of light olefins in the MTO reaction due to its unique structure. It features super cavities and 8-membered ring (8-MR) windows,[23] with the window dimensions of SAPOs being intimately related to the product distribution thanks to the shape selectivity features. For instance, a narrow 8-membered ring (8-MR) pore opening hinders the diffusion of aromatic molecules and branched hydrocarbons with high carbon numbers (C_n-H_m, $n > 4$), achieving a high selectivity for C_2–C_4 olefins of approximately 90%.[24] While SAPO-34 demonstrates excellent catalytic performance in the MTO process, it faces challenges with deactivation due to coke formation. The narrow channels, beneficial for selectivity, make SAPO-34 particularly susceptible to this issue as larger hydrocarbons and coke precursors struggle to diffuse out. Coke formation in the MTO process is driven by the physicochemical properties of the catalyst and the reaction conditions. It occurs in different stages; the interactions between hydrocarbon intermediates and acid sites, particularly Brønsted and Lewis acid sites, lead to pore blockage.[25] Tuning the strength and amount of acid sites is then crucial for optimizing the performance of SAPO-34 in the MTO reaction. Strong acid sites are necessary to catalyse the methanol transformation, but excessively strong sites can shift the product distribution toward undesired by-products.[26] Nevertheless, the weak surface acid sites alone are unable to transform the mono-olefin into aromatics.[27] Therefore, the weak acidic sites prevent various hydrogen transfer reactions, which may cause saturated aliphatic and aromatic formation.[28] The acidity of SAPO-34 is then directly related to Si incorporation in the framework; a lower Si content and acid site density enhance its catalytic performance and coke resistance in the MTO reaction.[29] SAPO-34 zeolites with a large number of acid sites can result in a serious secondary hydrogen transfer reaction, while SAPO-34 zeolites with a lower amount of acid sites can also cause the incomplete conversion of methanol during the MTO reaction.[30] It is of great significance to control the coordination mode of silicon atoms in SAPO frameworks to improve their performance in MTO reactions. The acidic sites could be controlled by the ratio of raw materials,[31,32] crystallization temperatures,[33] crystallization times,[34] the type of silicon source,[35] and the OSDA.[36,37]

The relationship between the number of acid sites and the silicon content is not straightforward since it is controlled by at least two Si incorporation mechanisms into the SAPO framework.[38] For instance, Li *et al.*[39] used three silica sources, TEOS, silica sol and fumed silica, and found that using fumed silica as a Si source, the sample had the highest bulk Si concentration while the highest acidity and the smallest particle size were obtained by using TEOS. These two lattice properties were found to improve product distribution and selectivity toward C_2= and C_3= olefins. Organic compounds, *i.e.*, OSDAs, play an important role as well, in the crystal size and morphology.[36] The action of an organic compound in AlPO or SAPO synthesis is well known for its role as an SDA, a space filling agent, and a charge compensating agent.[40] SAPO molecular sieves can then be prepared using various OSDAs such as tetraethylammonium hydroxide (TEA[+]), dipropylamine (DPA), diethylamine (DEA), morpholine, and triethylamine (TEA). However, different physicochemical properties might be obtained according to the type of OSDA and its concentration during the preparation.[36–41] We have previously investigated the role of OSDAs in the hydrophilic properties of AlPO-5 and SAPO-5 (AFI-structure) using neutral amines and positively charged ammoniums.[42,43] Using advanced nuclear magnetic resonance (NMR) spectroscopy, we elucidated the critical role of OSDAs in directing the organization of the inorganic framework in aluminophosphates. The size, shape, rigidity, hydrophobicity, and the number and/or location of the positive charges all influence the structure direction phenomenon.[44]

In this work, we will focus on the role of the OSDA's charge in the properties of SAPO-34 using two different OSDAs, TEA and TEA[+], aiming to control silicon distribution, acidity and thus catalytic properties, evaluated in the MTO reaction.

Experimental section

Materials

The chemical reagents used were: aluminium isopropoxide Al(OiPr)$_3$, pseudoboehmite, tetraethylammonium hydroxide (TEA[+], 35% in water), triethylamine (TEA), phosphoric acid

This journal is © The Royal Society of Chemistry 2026

Catal. Sci. Technol., 2026, **16**, 1400–1410 | **1401**

(H_3PO_4, 85% in water) and colloidal silica (SiO_2, Ludox HS-30, 30% in water). All chemicals were purchased from Sigma-Aldrich. Ultrapure water (Millipore Milli-Q grade) with a resistivity of 18.0 MΩ was used in all experiments, and chemicals were used without further purification.

Synthetic procedures

The sample synthesized with tetraethylammonium was obtained following a procedure developed in our group with a gel composition of $1Al_2O_3 : 2P_2O_5 : 2TEA_2O : 0.6SiO_2 : 75H_2O$. Typically, 2.94 g of $Al(OiPr)_3$ was completely dissolved under stirring for 1 h in a mix of H_2O (0.75 g) and TEA^+ (OH^-) (12 g). Then, 3.3 g of H_3PO_4 was slowly added in a drop-wise manner with continuous stirring for 2 hours. Finally, 0.86 g of colloidal SiO_2 was added and kept under stirring for 2 more hours. The resulting solution was transferred in a Teflon-lined ceramic autoclave (100 ml). A microwave treatment of the suspensions was carried out using an Anton Paar Synthos 5000 microwave reactor in a temperature-programmed mode (3.5 min to reach 200 °C with a power of 1000 W and maintained for 1 h before cooling down to room temperature).

The sample synthesized with triethylamine was obtained *via* a classical hydrothermal method with a molar composition of $1Al_2O_3 : 0.8P_2O_5 : 3TEA_2O : 0.6SiO_2 : 50H_2O$. Firstly, 2.8 g of pseudoboehmite was mixed with 13 g of distilled water, and 5.1 g of TEA (99%) was added to the solution under stirring for 1 h until complete dissolution. Then, 3.1 g of phosphoric acid (85%, aqueous solution) was added dropwise. The mixture was stirred for 2 h, and then 1 g colloidal SiO_2 was added and stirred. After one hour, the resulting synthesis gel was crystallized at 200 °C for 48 hours in a 50 mL Teflon-lined autoclave.

The crystalline products were separated by centrifugation (20 000 rpm, 45 min, 15 °C). The solid materials were purified by a series of centrifugation and ultrasonic re-dispersion in distilled water to reach a pH of 8 for the liquid phase. The crystalline products were dried at 110 °C overnight and calcined with a heating ramp of 1 °C min^{-1} at 600 °C for 8 h before characterization. The chemical composition and the synthesis parameters are summarized in Table 1. In this manuscript, the sample synthesized using the positively charged OSDA (TEA^+) is named P-AS or (C), while the sample with the neutral OSDA (TEA) is called N-AS or (C); "AS" and "C" were added to the names to define as-synthesized (AS) and calcined (C) samples, respectively.

Characterization

The crystallinity of the samples was characterized using a PANalytical X'Pert PRO diffractometer with Cu Kα radiation (λ = 0.15418 nm), 40 mA, 45 kV, a step size of 0.02°, a scan speed of 1° min^{-1}, and a 2θ range of 5–25°. The unit-cell parameters were obtained by Le Bail refinements performed with the GSAS-II program.[45]

Scanning electron microscopy (SEM) was performed using a Tescan Mira I LMH operating at 30 kV and a JEOL JSM-IT800 Schottky field emission scanning electron microscope at 0.8 kV and 10 nA. ImageJ[46] software was used to analyze the particle size distribution according to the SEM images.

Thermogravimetric analyses (TGA) were performed using a NETZSCH STA 449F3 system in air in the temperature range of 35–800 °C with a heating rate of 10 °C min^{-1}. A Micrometrics ASAP 2020 was used for recording N_2 adsorption/desorption isotherms at −196 °C, manometrically up to 1 bar. The samples were degassed overnight at 350 °C (heating rate of 1 °C min^{-1}) using ultrapure N_2 under vacuum prior to the measurement. The specific surface area (SSA) was calculated by the multipoint Brunauer–Emmett–Teller (BET) method in the relative pressure range of $0.05 < P/P^0 < 0.25$. Micropore volumes were determined by the t-plot method and mesopore volumes were obtained by the BJH desorption method.[47] Inductively coupled plasma mass spectrometry (ICP-MS) measurements were performed using a 7900 ICP-MS from Agilent Technologies.

FT-IR analysis was performed using a Nicolet iS 10 (Thermo Scientific, USA), equipped with a DTGS detector. The samples were pressed into self-supported wafers of 30 (±1) mg and 16 mm diameter under a load of 2.5 tons cm^{-2}. The pellets were activated *in situ* at 450 °C for 2 h under high vacuum (10^{-6} mbar), using a heating ramp of 5 °C min^{-1}. The temperature was monitored using a thermocouple in contact with the cell heater. After activation, the samples were cooled to room temperature under vacuum. FT-IR spectra were recorded before and after deuterated acetonitrile (d$_3$-acetonitrile, CD_3CN) chemisorption at room temperature in the range of 4000–600 cm^{-1}, with an optical resolution of 4 cm^{-1}, with 128 scans at a pressure of 10^{-6} mbar. 2.5 mbar CD_3CN was dosed stepwise into the IR cell through a calibrated volume, using two pressure transducers to monitor both the line pressure and the probe aliquots. Adsorption was carried out until saturation was reached; saturation is defined as the concentration at which further dosing did not increase the integrated area of the $v(C≡N)$ bands associated with protonated (Brønsted, 2294 cm^{-1}) and coordinated (Lewis, 2322 cm^{-1}) species. After saturation, the sample was equilibrated for 15 min and subsequently evacuated at 25 °C (10^{-6} mbar) for 1 h to remove physisorbed molecules. The Lambert–Beer law ($A = \varepsilon \cdot N \cdot \rho$) was used to evaluate the total number of acid sites considering the protonated species. Note that A is the absorbance, ε, the molar extinction

Table 1 Chemical composition of precursor suspensions used for the synthesis of N-AS and P-AS samples

Sample	Gel molar composition	Temperature (°C)	Time (h)
N-AS	$1Al_2O_3 : 0.8P_2O_5 : 3TEA_2O : 0.6SiO_2 : 50H_2O$	200	48
P-AS	$1Al_2O_3 : 2P_2O_5 : 2TEA_2O : 0.6SiO_2 : 75H_2O$	180	1

coefficient (cm mmol^{-1}), N, the concentration of the vibrating species (mmol g^{-1}), and ρ, the areal density of the disk (mg cm^{-2}). The values of molar extinction coefficients used were ε = 2.05 cm mmol^{-1} for CD$_3$CN on Brønsted acid sites (BASs) and ε = 3.6 cm mmol^{-1} for CD$_3$CN on Lewis acid sites (LASs).[48] The FTIR spectra were processed using 'OMNIC' software.[49] Baseline subtraction was performed prior to peak integration by subtracting the activated (degassed) sample spectrum from the spectrum obtained after d$_3$-acetonitrile adsorption.

Magic-angle spinning nuclear magnetic resonance (MAS NMR) spectra of ^{27}Al, ^{31}P, ^{13}C and ^{29}Si nuclei were recorded with single pulse experiments on a Bruker Avance 500 MHz (11.7 T) spectrometer at ^{27}Al, ^{31}P and ^{29}Si Larmor resonance frequencies of 130.30, 202.42 and 99.35 MHz, respectively. 3.2 mm zirconia rotors were used, and the spinning rate was fixed to 14 kHz. The ^{27}Al MAS NMR spectra were recorded using a pulse width of 1.75 μs ($\pi/6$), and 4096 scans were acquired for all the samples with a recycle delay of 1 s. The ^{31}P MAS NMR spectra were recorded using a pulse width of 5 μs ($\pi/2$), and 256 scans were acquired with a recycle delay of 20 s. The ^{29}Si MAS NMR spectra were acquired using a pulse width of 2.33 μs ($\pi/3$), and 11 264 scans were acquired with a recycle delay of 20 s. The ^{13}C{^{1}H} cross-polarization CPMAS NMR spectra were obtained using a contact time of 5 ms, and 256 scans were acquired with a recycle delay of 20 s. The chemical shifts were calibrated with tetramethylsilane (TMS) at 0 ppm for ^{13}C, ^{1}H and ^{29}Si, while H$_3$PO$_4$ was used as a reference for ^{31}P; ^{27}Al NMR spectra were referenced using a 0.1 M Al(NO$_3$)$_3$ aqueous solution at 0 ppm.

Raman spectra were recorded using a Jobin Yvon LamRAM HR spectrometer. An argon laser at 532 nm was focused on the sample powders with a microscope using a 50× objective lens. The power of the laser beam was approximately 4 mW. The back-scattered radiation was collected, and the spectral resolution was approximately 0.5 cm^{-1}.

Catalytic test

The performance of the SAPO samples in the MTO reaction was tested using an online sampler's fixed bed atmospheric pressure microreactor device. 0.1 g of catalyst (35–60 mesh) was filled into a quartz tube with an inner diameter of 6 mm as a support reaction tube. N$_2$ with a pressure of 0.45 MPa was introduced to check the air tightness of the reaction device pipes and connectors. Then the catalyst was activated for 1 h at 550 °C in air with a flow rate of 40 mL min^{-1}, and then cooled to the reaction temperature of 470 °C under a flow of N$_2$ (55 mL min^{-1}). After activation, a methanol and water mixture (50 vol%/50 vol%) was introduced at atmospheric pressure with a mass space velocity of 1.5 h^{-1}. The data collected by the online chromatography workstation were used to determine the composition and distribution of the products by a standard external method. With intake sampling, a chromatograph (Chromatic-Crystal GC-9000) uses a PONA capillary column (50 m × 0.2 mm) and a flame

ionization detector (FID) to detect the reactant and products. The methanol conversion rate is calculated using the following equation:

$$\text{Conv}_{\text{CH}_3\text{OH}}(\%) = \left(1 - \frac{A + 2 \times A'}{A_0}\right) \times 100\%$$

where A_0 is the methanol peak area measured without catalyst loading, A is the methanol peak area measured during the reaction, and A' is the DME (dimethyl ether) peak area measured during the reaction. In the MTO reaction, the tail gas products are mainly C$_1$–C$_4$ alkanes and C$_2$–C$_4$ light olefins. The product selectivity is calculated using the following equation:

$$\text{Sel C}_2 - \text{C}_4 = \frac{\text{Methanol equivalent of light olefin products}}{\text{Total product methanol equivalent}}$$
$$= \frac{\sum_0^i n_i X_i}{\sum_0^j n_j X_j} \times 100\%$$

where n is the number of carbon atoms of the product, i denotes ethylene, propylene, and butylene, and X is the mass fraction of the product.

Results and discussion

Fig. 1 presents the XRD patterns of the as-synthesised and calcined SAPO-34 samples prepared with both OSDAs. Characteristic peaks of the CHA structure were observed at 9.6°, 12.9°, 16.2°, and 20.9°, reflecting the high crystallinity of all samples.[8] No loss in crystallinity was observed when the as-synthesized samples were heated at 600 °C in order to remove the organic molecules, confirming their thermal stability under calcination conditions; however, the intensity and the width of peaks were different depending on the
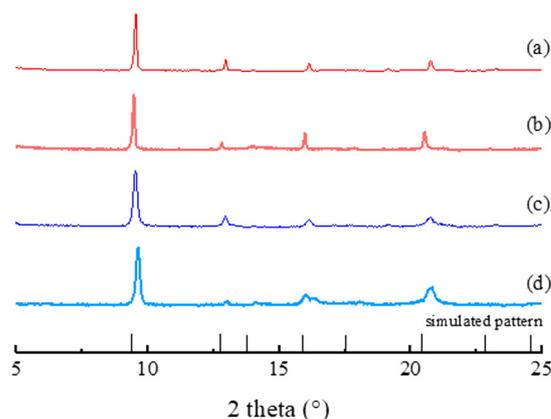

Fig. 1 Powder XRD patterns of N–C (a), N–AS (b), P–C (c), and P–AS (d) samples. Black lines at the bottom show the Bragg peaks of the simulated CHA-structure.[8]
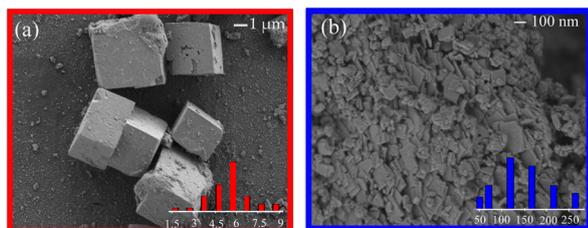
Fig. 2 SEM images of N-C (a) and P-C (b) and their particle size distributions (bottom).

Table 3 Elemental composition of samples of N-C and P-C

Sample	Composition[a]	Si/Al	(Si + P)/Al	Si/(Si + P + Al)
N-C	$Al_{0.40}P_{0.38}Si_{0.05}O_2$	0.19	0.75	0.11
P-C	$Al_{0.40}P_{0.44}Si_{0.002}O_2$	0.12	1.20	0.06

[a] Measured by ICP-MS.

OSDA used. The broader XRD peaks of sample P-C suggest a smaller particle size, as confirmed by SEM images, *vide infra*. The unit cell parameters and volumes of all samples (Table 2) reveal some differences depending on both the OSDA (TEA *vs.* TEA$^+$) and the as-synthesized *vs.* calcined conditions. N-AS and P-AS exhibit slightly larger *a* and *c* lattice parameters (2458 and 2417 Å^3), resulting in an increase in the unit cell volume compared to the calcined samples (2383 and 2375 Å^3). This expansion is consistent with the presence of the organic species within the framework, which, once removed upon calcination, leads to a slight contraction of the structure. Notably, SAPO-34 synthesized with the neutral OSDA (TEA) shows a larger unit cell volume than the corresponding TEA$^+$ samples, both before and after calcination, 2458 and 2383 Å^3 for N-AS and N-C *vs.* 2417 and 2375 Å^3 for P-AS and P-C. This suggests that the OSDA may induce slight modifications in the framework, possibly due to weaker interactions with the framework.

Sample N-C exhibits a well-defined cubic morphology with sharp edges and uniform size distribution Fig. 2(a). The average crystal size is around 5–6 μm, as indicated by the red histogram. This morphology is characteristic of SAPO-34 with the chabazite (CHA) topology and reflects relatively slow nucleation and crystal growth rates typically associated with smaller, neutral amine OSDAs like TEA. In contrast, a very different morphology for P-C crystals is observed; the particles are significantly smaller, with an average size of 100–200 nm, *cf.* blue histogram, Fig. 2(b). The particles are densely packed and exhibit an aggregated, plate-like morphology, suggesting higher nucleation rates that lead to a reduced crystal growth rate.[35] TEA$^+$, in the presence of OH$^-$ (Brønsted base), accelerates nucleation while reducing the crystal growth rate. In contrast, TEA (Lewis base), limits the number of nuclei, promoting the crystal growth. Note that P-C crystals exhibit an anisotropic morphology and their particle size was determined by measuring the in-plane

length of the particles considering the high surface dimension in the SEM images.

Sample N-C has a higher silicon content compared to P-C (Table 3), as measured by ICP-MS. Following the concept developed by Barthomeuf[19] based on topological density considerations, the number of isolated silicon atoms correlates with the silicon content; the maximum Si content at which all silicon atoms exist as isolated species in SAPO-34 corresponds to a Si/Al ratio of 0.108.

In this context, an isolated silicon atom refers to a silicon tetrahedron that has no silicon neighbours in either the first or second coordination sphere of T atoms. Based on the elemental composition, both samples may exhibit silicon islands Si(nAl) where $0 < n < 3$, and this is confirmed by the ^{29}Si NMR study (Fig. 5).

Thermogravimetric analyses (TGA) were performed to verify the incorporation of OSDA molecules into the structure of the as-synthesised samples and their subsequent complete removal after calcination, prior to the use of SAPO-34 materials in catalytic reactions. The TGA profiles and their corresponding data are shown in Fig. 3. The results display three distinct weight losses (I, II, and III) within the 50–800 °C range. The first weight loss (I), at temperatures below 250 °C, is attributed to water desorption. The second weight loss (II), between 250 and 450 °C, is due to the decomposition of the OSDA. Finally, the third weight loss (III), at temperatures above 450 °C, is associated with the removal of additional organic residues occluded in the channels and cages of SAPO-34. As shown in Fig. 3, sample N-AS exhibits a larger weight loss below 250 °C compared to P-AS, 4% and 2%, respectively. This is due to a higher amount of water physically adsorbed on the external surface. Comparing the two samples, the weight losses occur over different
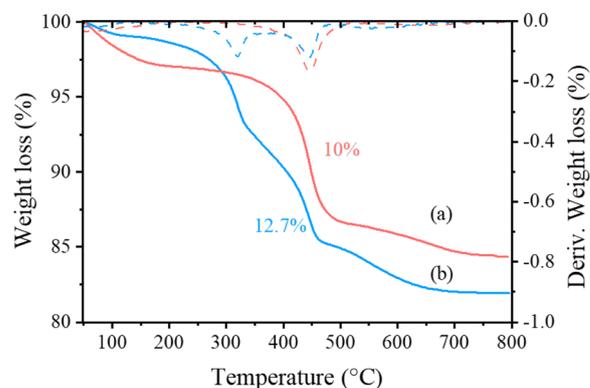
Table 2 Unit cell parameters and corresponding unit cell volumes of samples N-AS, N-C, P-AS and P-C

Sample	*a* (Å)	*c* (Å)	Volume (Å^3)
N-C	13.61	14.85	2383
N-AS	13.80	14.92	2458
P-C	13.56	14.90	2375
P-AS	13.73	14.81	2417

Fig. 3 TG and DTG data of N-AS (a) and P-AS (b) samples.

1404 | *Catal. Sci. Technol.*, 2026, **16**, 1400–1410

This journal is © The Royal Society of Chemistry 2026

temperature ranges, which is due to both differences in molecular size and OSDA–framework interaction.[50] During the OSDA removal process, the weight loss between 250 and 450 °C is approximately 10 wt% for N-AS and 12.7 wt% for P-AS samples. From the DTA curves shown in Fig. 3, the decomposition of TEA$^+$ occurs in two distinct phases, at ~330 °C and ~440 °C, while the decomposition of TEA is associated with a single peak at ~450 °C. While this may be due to the different decomposition mechanisms of the quaternary ammonium compared to amines, the occurrence of different environments and particle size distributions must be considered as well. The amount of OSDA per cage was calculated based on the elemental composition (Table 3) and the topological structure of the samples. While 1.2 molecules of TEA$^+$ are found in a unit cell, 1.6 molecules of TEA occupy the same space approximatively, Table S2. The incorporation of TEA and TEA$^+$ molecules inside the frameworks of SAPO-34 is confirmed also by ^{13}C MAS NMR spectroscopy. The spectra of N-AS and P-AS consist of two signals at 13.9 and 53.1 and at 13.8 and 59.9 ppm, which correspond to –CH$_3$ and N–CH$_2$–in N-AS and P-AS, respectively[51] (Fig. S1A).

The nitrogen (N$_2$) adsorption–desorption isotherms of the SAPO-34 samples are shown in Fig. 4. Both samples exhibit type-IV(a) behaviour with an H$_3$ hysteresis loop appearing at a relative pressure of 0.4–1 (ref. 52), indicating the coexistence of microporosity and inter-crystalline mesoporosity. The N$_2$ uptake in the low-pressure region (0–0.04) corresponds to the filling of intrinsic micropores associated with the CHA framework. The micropore volume is greater in P-C than in N-C, 0.28 and 0.20 cm^3 g^{-1}, respectively. This is due to the presence of more defects in the sample synthesized using TEA$^+$. The pore size distribution of N-C and P-C analysed through the non-local density functional theory (NLDFT) model is shown in Fig. S2. Both materials exhibit a primary peak at 0.6 nm, confirming the predominance of micropores within both structures. These
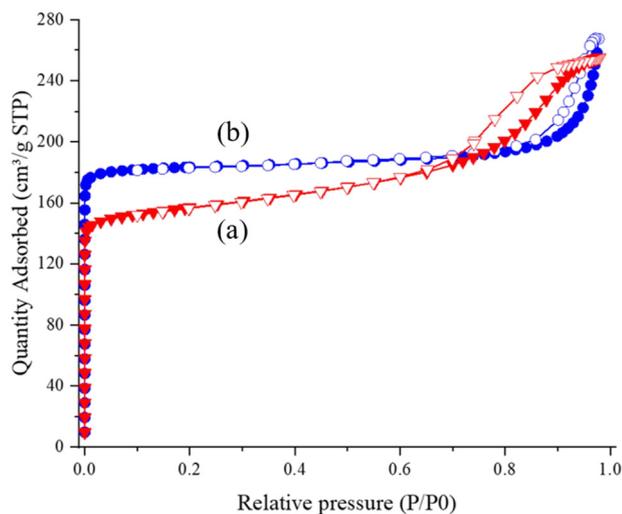
Table 4 Textural properties of samples N-C and P-C determined from N$_2$ sorption isotherms

Sample	S_{BET} (m^2 g^{-1})	V_{micr} (cm^3 g^{-1})	V_T (cm^3 g^{-1})
N-C	619	0.20	0.40
P-C	775	0.28	0.44

values align with the characteristic pore dimensions of SAPO-34, which possesses a CHA framework with an open pore size of approximately 0.38 nm and a cage size of 0.73 nm.[8] P-C exhibits a sharper and more intense peak, suggesting a more uniform microporous structure, whereas N-C displays a broader distribution with a slightly lower peak intensity, indicative of a more heterogeneous pore network. The textural properties of N-C and P-C are reported in Table 4.

Solid-state NMR spectroscopy was performed to elucidate the coordination environments of the frameworks before and after calcination of the samples. The environments of Al and Si are shown in Fig. 5, while ^{13}C and ^{31}P NMR spectra of the samples are shown in Fig. S1 (Table S1). The deconvolution of the ^{27}Al MAS NMR spectra was performed using the CzSimple model available in DMfit software,[53] while for the ^{13}C, ^{29}Si and ^{31}P NMR spectra, Lorentzian peaks were used. The ^{13}C MAS NMR spectra (Fig. S1) confirm the incorporation of the OSDAs TEA and TEA$^+$ into SAPO-34. The chemical shifts of the carbon species align well with the expected signatures for the respective OSDAs. The signal at 59.8 ppm in P-AS corresponds to the methylene group adjacent to the quaternary nitrogen, reflecting a more constrained and framework-interacting configuration.[54]

The ^{27}Al MAS NMR spectra of the SAPO-34 samples synthesized with TEA and TEA$^+$ reveals distinct aluminium coordination environments before and after calcination. In N-AS, the spectrum shows a peak at 41.9 ppm, corresponding to tetrahedrally coordinated aluminium (Al^{iv}), with a relative percentage of 53%. An additional peak at 10.5 ppm appears with a relative percentage of 47%, attributed to penta-coordinated species (Al^V). The ^{27}Al MAS NMR spectrum of N-C reveals distinct differences in aluminium coordination environments, reflecting the structural reorganization induced by the removal of the OSDA. N-C still exhibits a strong and sharp signal at 43.2 ppm, assigned to tetrahedrally coordinated aluminium (74%); however, the peak at 11 ppm corresponding to penta-coordinated Al decreases to 26%.

This reorganization affects the Si distribution, cf. ^{29}Si NMR spectra (Fig. 5B). The loss of intensity of the penta-coordinated Al species and the consequent rearrangement of the Si and Al atoms may be explained by the presence of some amorphous silicon in the as-synthesized sample.

The P-AS sample also shows a dominant tetrahedral Al signal at 43.2 ppm. This is accompanied by penta- and hexa-coordinated Al atom (Al^V and Al^{VI}) signals at 13.9 and −7 ppm, respectively, suggesting a higher degree of framework disordering in the presence of TEA$^+$. The latter peak indicates the presence of a small amount of octahedral aluminium
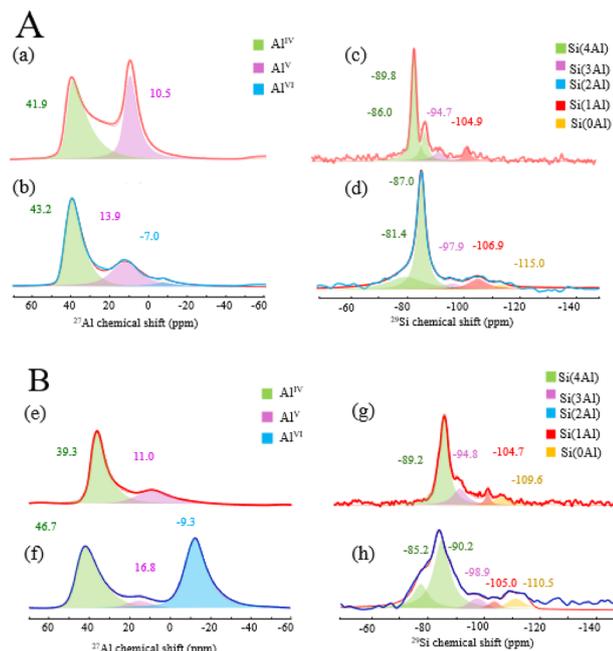

Fig. 4 N$_2$ adsorption/desorption isotherms of N-C (a) and P-C (b).

This journal is © The Royal Society of Chemistry 2026

Catal. Sci. Technol., 2026, **16**, 1400–1410 | **1405**

Fig. 5 (A) Solid-state ^{27}Al MAS NMR spectra (left) and ^{29}Si MAS NMR spectra (right) of N-AS (a and c) and P-AS (b and d); (B) solid-state ^{27}Al MAS NMR spectra (left) and ^{29}Si MAS NMR spectra (right) of N-C (e and g) and P-C (f and h).

atoms formed by an additional coordination of two water molecules to tetrahedrally coordinated framework aluminium atoms or by extra-framework aluminium species. Its relative percentage is low, ~5%. However, P-C shows a peak at −9.3 ppm with a significantly high intensity and a relative percentage of 51%, Table 5. It is also worth noting that Al^{VI} does not appear in N-C, while in P-C, a relatively high amount is observed. This reflects a higher local ordering in N-C compared to a certain disorder in the Al distribution induced by TEA$^+$.

The ^{31}P MAS NMR spectra of the as-synthesised samples show an intense peak attributed to PO$_4$ tetrahedra for all the samples, before and after the calcination between −28 and −31 ppm; note that a peak broadening is observed in P-C (Fig. S1). The ^{31}P NMR isotropic chemical shift, being dependent on both the chemical modifications and the P–O–Al bond angles as well as the presence of P–OH defects, aligns with the numerous environments observed in the ^{27}Al NMR spectra.[55]

The ^{29}Si MAS NMR spectra of the as-synthesized SAPO-34 samples reveal distinct silicon coordination environments that reflect the influence of the OSDA on the silicon incorporation mechanism. In these materials, the silicon distribution is typically identified by the number of neighbouring aluminium atoms; for instance, a peak in the green region at around −82 to −91 ppm is typically assigned to Si(4Al), indicating that silicon is fully incorporated into the framework surrounded solely by aluminium atoms. In contrast, peaks found at more negative chemical shifts (pink to blue regions) correspond to mixed silicon–aluminium environments—Si(3Al) and Si(2Al), while the red and yellow regions (e.g., −103 to −115 ppm) indicate environments with fewer aluminium neighbours, such as Si(1Al) and even predominantly silica-like domains Si(0Al).[56] These latter environments often emerge when secondary silica domains, defects, or disordered regions form during synthesis and after the OSDA removal.[57] The ^{29}Si MAS NMR spectra of the SAPO-34 samples reveal complex environments of silicon that evolve with calcination. In the N-AS material, the spectrum exhibits a broad and complex pattern spanning from −85 to −104 ppm, with an intense peak in the −86 to −90 ppm range, corresponding to Si(4Al). Thus, two broad peaks and a weak peak appearing at −94.7 ppm and at −104.9 ppm are assigned to Si(3Al) and Si(1Al). These peaks are consistent with the operation of both SM$_2$ and SM$_3$ substitution mechanisms. Upon calcination, both samples undergo a redistribution of silicon environments. In N-C, the reduction of the Si(4Al) contribution from 80% to 64% is accompanied by a redistribution toward silicon-island environments, and a new Si(0Al) signal emerges with a relative intensity of 9%. In contrast, the sharp peak at −90 ppm in the P-C sample, corresponding to the Si(4Al) environment, remains unchanged after calcination (82%). The redistribution of Si in this sample occurs mainly within the silicon-island environments; it is reflected by small variations in the Si(3Al), Si(2Al), and Si(0Al) components. Then, calcination may be promoting the reorganization of silicon environments toward more stable configurations upon the removal of organic species.[57]
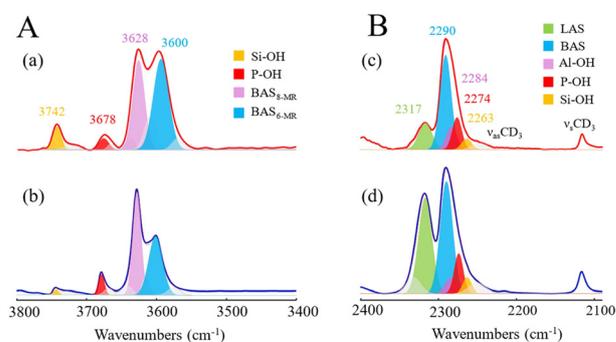
Table 5 The ^{27}Al, ^{31}P and ^{29}Si relative percentage in samples N-AS, P-AS, N-C and P-C

Sample	^{27}Al chemical shift			^{29}Si chemical shift			
	Al^{IV}	Al^{V}	Al^{VI}	Si(4Al)	Si(3Al)	Si(1Al)	Si(0Al)
N-AS	53	47	—	80	10	9	—
P-AS	61	33	5	83	2	12	2
N-C	74	26	—	64	19	6	9
P-C	41	6	51	82	5	2	12

Fig. 6 FTIR spectra of the OH-stretching region (A) and spectra collected after CD$_3$CN dosing at RT in the region between 2400 and 2100 cm^{-1} (B) on N-C (a and c) and P-C (b and d).

Table 6 Concentration of Brønsted acid sites in the 8-MR and 6-MR in the –OH region and Lewis and Brønsted acid sites of adsorbed CD_3CN, determined by FTIR spectroscopy

Sample	Brønsted sites 8-MR	Brønsted sites 6-MR	Lewis sites (µmol CD_3CN per g)	Brønsted sites (µmol CD_3CN per g)	Total concentration of acid sites (µmol CD_3CN per g)
N-C	189	147	41	191	232
P-C	271	108	143	275	418

The OH stretching regions of the FT-IR spectra of the samples outgassed at 450 °C are shown in Fig. 6A. Two weak bands are observed at around 3747 and 3678 cm^{-1} attributed to Si–OH and P–OH species, respectively. The sample N-C presents a more intense peak at 3747 cm^{-1}, indicating the presence of a significant amount of isolated hydroxyl groups. Meanwhile, the peak assigned to P–OH is more intense for P-C, in agreement with the ^{31}P NMR spectra (Fig. S1). Two additional peaks with intense absorption at about 3627 and 3600 cm^{-1} are also observed for both samples, corresponding to bridging hydroxyl groups (Si–OH–Al) associated with the Brønsted acid sites;[58] the first peak is assigned to the BAS_{8-MR} and the second one is attributed to the BAS_{6-MR}. As is observed in N-C, the BAS_{8-MR} is less intense than that of P-C and this may explain the variation of silicon distribution after the calcination as shown in the ^{29}Si NMR spectra, Fig. 5. When the OSDA is removed, the silicon in the 8-MR may be impacted, while the silicon present in the 6-MR remains unaltered. The relative percentages of species are reported in Table 6. In order to discriminate Lewis acid sites (LASs) from Brønsted acid sites (BASs), CD_3CN has been used as a probe molecule, Fig. 6B. The peaks associated with Brønsted acid sites decrease upon adsorption and disappear completely for P-C. In contrast, in N-C, these sites are not fully occupied (Fig. S3). The different extents of Brønsted acid site occupation observed in the samples are attributed to variations in acid strength, site accessibility, and crystal size. In P-C, the complete disappearance of the corresponding IR peaks suggests full occupation of the Brønsted acid sites and indicates a high density of accessible sites or stronger interactions with CD_3CN. In contrast, in N-C, some acid sites remain unoccupied, likely due to steric hindrance or lower acid strength. These findings highlight the crucial role of the organic OSDA in determining the acidity of SAPO-34.

As illustrated in Fig. 6B, the CD_3CN-saturated samples show different peaks attributed to the symmetrical vibration of CD_3, the interaction of the probe with BASs and the interaction with LASs, respectively. The presence of a $v(C\equiv N)$ stretching band at 2275–2290 cm^{-1} is associated with the interaction of CD_3CN with zeolite defects (i.e., Si–OH, P–OH and Al–OH), whereas the presence of physisorbed and liquid phase CD_3CN is characterized by the bands at 2265 cm^{-1} and 2250 cm^{-1}, respectively. The bands at around 2270, 2279 and 2286 cm^{-1} are assumed to correspond to CN groups interacting with terminal Si–OH, P–OH and Al–OH groups or defect sites, respectively, while the peak in the 2251–2256 cm^{-1} region is assigned to the asymmetric stretching mode of CD_3 groups, together with a symmetric stretching mode

found at 2114 cm^{-1}. The number of Lewis acid sites was calculated from the area of the band at 2322 cm^{-1} by adopting an extinction factor of 3.6 cm µmol^{-1}, while the number of Brønsted acid sites was calculated by adopting an extinction coefficient of 2.05 cm µmol^{-1}.[48] The concentrations of Lewis and Brønsted acid sites are presented in Table 6. The comparison between N-C and P-C reveals some differences in both the nature and concentration of their acid sites. The IR spectra of adsorbed CD_3CN show that N-C exhibits a dominant band at 2294 cm^{-1}, corresponding to Brønsted acid sites (191 µmol g^{-1}), along with a weaker feature at 2322 cm^{-1} attributed to Lewis acid sites (41 µmol g^{-1}). In contrast, P-C displays a more intense band at 2322 cm^{-1}, reflecting a significantly higher concentration of Lewis acid sites (143 µmol g^{-1}), while Brønsted acidity is also slightly increased (275 µmol g^{-1}). Overall, the total acid site concentration is substantially greater in P-C (418 µmol g^{-1}) compared to N-C (232 µmol g^{-1}). These findings suggest that TEA favours stronger Brønsted acidity with fewer Lewis sites, whereas TEA$^+$ promotes a higher density of both acid types. However, the Lewis acid sites in the P-C sample appear to be slightly weaker on average, as suggested by the small shift in wavenumber. These differences in acid site distribution and strength are particularly relevant for methanol-to-olefin (MTO) catalysis. In this process, strong Brønsted acid sites are essential for the initial activation of methanol and the formation of the first carbon–carbon bonds.

The MTO reaction was carried out to evaluate the catalytic performance of the samples. The methanol conversion and ethylene/propylene ratio (E/P) selectivity are presented in
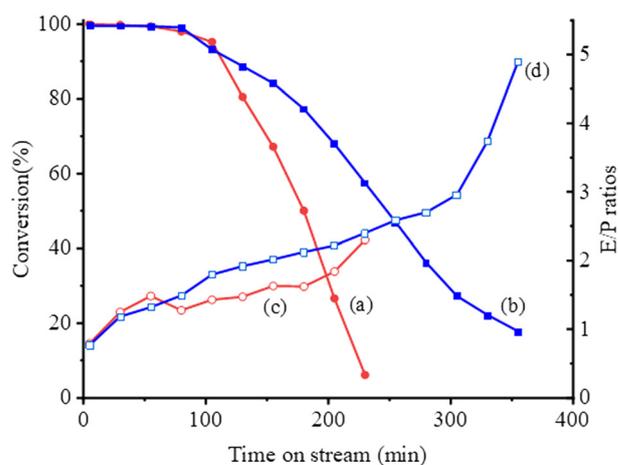

Fig. 7 Methanol conversion of samples N-C (a) and P-C (b) and E/P ratio of samples N-C (c) and P-C (d).

Fig. 7A. For P-C, the methanol conversion decreased to 90% after 55 minutes, 20% after 125 minutes, and 20% after 340 minutes. Comparing the two samples at the catalyst deactivation stage shows that the N-C sample exhibits a deactivation rate of 0.71% min^{-1}, whereas the P-C sample shows a rate of 0.33% min^{-1}, indicating superior catalytic kinetics for the latter. This confirms the intimate relationship between the catalyst size and its lifetime.[59] For both samples, deactivation starts after 105 minutes at different rates due to differences in diffusion features. Interestingly, the ethylene-to-propylene ratio for P-C is higher than that of N-C during the steady and deactivation stages (after 85 minutes) reaching 4.9. In contrast, N-C maintained a more balanced product distribution, with E/P ratios stabilizing at around 1.5–2.3 from 55 to 230 minutes. This behaviour reflects the combined influence of the crystal size and the Brønsted acidity, leading to a reduced extent of secondary transformations. This agrees with previous studies showing that smaller SAPO-34 crystals favour higher E/P ratios due to shorter diffusion paths and lower propensity for olefin interconversion.[60,61] In terms of ethylene and propylene selectivity, N-C demonstrates a similar selectivity compared to P-C, *i.e.* 85.4% *vs.* 80.6%. Additionally, N-C exhibits a higher C_3 hydrogen transfer index (HTI) of 0.03, *versus* 0.01 for P-C. This is attributed to its stronger surface acidity, which promotes hydrogen transfer reactions of light olefins to form alkanes. Furthermore, the use of TEA$^+$ leads to lower silicon incorporation and suppresses the formation of Si islands; nonetheless, the resulting nanosized crystals exhibit more accessible Brønsted and Lewis acid sites, which ultimately favours a longer catalytic lifetime.[62]

Additionally, the XRD patterns of the spent catalysts were collected after the MTO reaction (Fig. S4). The XRD patterns of the fresh and spent SAPO-34 catalysts show characteristic peaks of the CHA-topology, confirming the stability of the framework. However, the patterns show a broad peak at 27°, attributed to carbonaceous species.[63] TGA analysis, Raman and NMR spectroscopy were performed to investigate the coke content in the samples after the reaction. As shown in Fig. 8A, the coke content (mass loss after 300 °C) of P-C is higher than that of N-C (12.0 wt% *vs.* 7.6 wt%); similar combustion temperatures indicate a comparable coke composition, suggesting that the coke primarily deposits on the external surface. The build-up of coke deposits can also be elucidated from the Raman spectra (Fig. 8B). The spectrum of the N-C catalyst exhibits an additional band at 1536 cm^{-1}, which has been attributed to vibrations associated with the SAPO-34 framework itself.[64] In accordance with previous *in situ* UV-Raman studies,[65] the bands observed at approximately 1630, 1509, and 1420 cm^{-1} can be assigned to retained C_4^+ olefins confined within the SAPO-34 cages, which are known to accumulate when diffusion through the narrow 8-membered ring windows is limited. The distinct band at 1616 cm^{-1} is indicative of the presence of aromatic species, while the peak at 1386 cm^{-1} corresponds to polycyclic aromatic hydrocarbons (PAHs), such as
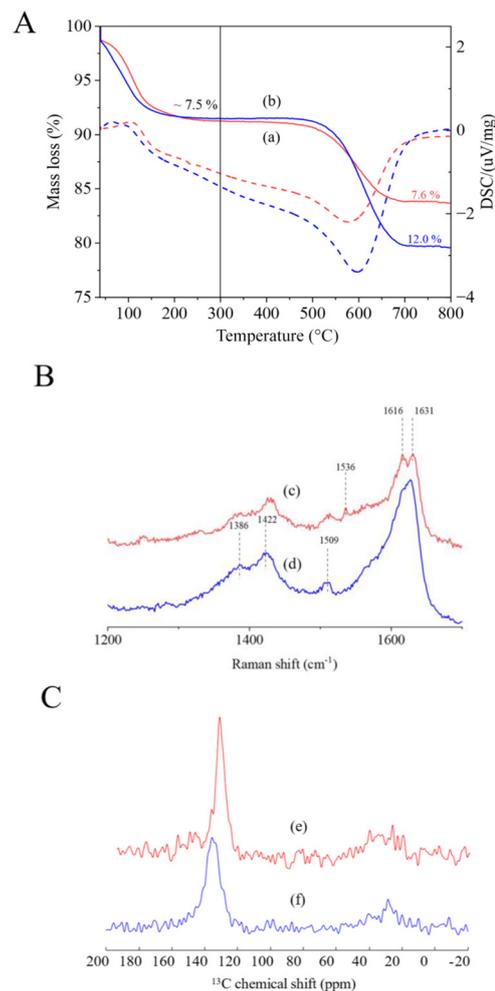

Fig. 8 (A) TG (solid line)/DSC (dashed line) curves, (B) Raman spectra, and (C) ^{13}C NMR spectra of samples N-C (a, c and e) and P-C (b, d and f) after the MTO reaction.

naphthalene. These findings suggest that the nature and location of coke species differ between the two catalysts: N-C favours the accumulation of olefinic and aliphatic residues in the pores leading to more rapid deactivation, while P-C tends to develop more aromatic, external coke due to its smaller crystal size and higher acidity.

^{13}C MAS NMR measurements were also performed (Fig. 8C). For both samples, strong signals occur, corresponding to aromatic carbon atoms (125–140 ppm) and alkyl carbon atoms bound to aromatic rings (12–30 ppm);[66] these signals indicate the formation of polyalkyl aromatics as dominant organic species.

The catalyst with larger crystal size (N-C) shows earlier deactivation compared to the nanocrystalline counterpart (P-C). These findings suggest that not only the amount, but also the location and nature of coke, are key factors governing catalyst longevity. In summary, although P-C produces more coke due to its higher acidity, its nanocrystalline nature and coke morphology enable superior diffusion and better resistance to deactivation, making it a more robust catalyst for MTO applications.

1408 | *Catal. Sci. Technol.*, 2026, **16**, 1400–1410

This journal is © The Royal Society of Chemistry 2026

Conclusions

In conclusion, we synthesized SAPO-34 molecular sieves using two different structure-directing agents: neutral triethylamine (TEA) and positively charged tetraethylammonium hydroxide (TEA$^+$). Our findings demonstrate that the OSDA charge plays a pivotal role in controlling both the amount and distribution of silicon within the SAPO-34 framework. The TEA-containing sample (N-C) exhibits a higher overall silicon content, with a higher portion forming Si islands which contribute to fewer but stronger Brønsted acid sites, and more pronounced hydrogen transfer reactions. In contrast, the use of TEA$^+$ for sample P-C favours a more homogeneous silicon dispersion leading to the formation of well-defined Si(4Al). These isolated Si–O–Al linkages are directly responsible for the generation of a greater number of Brønsted acid sites and improved acid site accessibility. The structural differences induced by the two OSDAs are validated by solid-state NMR and FT-IR spectroscopy. P-C exhibits higher total acid site concentration, while N-C shows stronger acidity, but lower acid site distribution. The enhanced acidity in P-C is further supported by the greater extent of CD$_3$CN adsorption on Brønsted and Lewis acid sites, suggesting both stronger interaction and higher site availability.

From a catalytic point of view, these structural and acidic characteristics translate into distinct performance profiles in the MTO reaction. While N-C shows higher initial selectivity toward light olefins (C$_2$–C$_4$) and greater hydrogen transfer activity, its faster deactivation is attributed to larger crystal size and more confined diffusion pathways, which promote coke formation. Conversely, P-C, despite having slightly lower initial selectivity, demonstrates superior catalyst stability and lifetime due to its nanoscale crystal size, larger external surface area, and higher number of acid sites, which together improve diffusion, mitigate coke deposition, and sustain higher methanol conversion over time. Overall, this study highlights the critical role of OSDA choice in shaping the framework structure, acidity, and catalytic behaviour of SAPO-34. By tuning the OSDA's charge and steric characteristics, it is possible to direct the mode of silicon incorporation, balance the density and strength of acid sites, and optimize the performance of SAPO-34 in acid-catalysed processes. These insights provide a valuable strategy for the rational design of SAPO catalysts with tailored properties for selective and stable MTO conversion.

Author contributions

S. Mintova, E. Dib and L. Pace conceived the project and designed the experiments. L. Pace designed, synthesized and characterized the materials. J. Wu carried out the catalytic test. M.-G. Geloso performed the Raman spectroscopy. D. Honorato-Piva acquired the SEM images. F. Dalena contributed to the FT-IR acquisition. The manuscript was written through contributions of all authors. All authors have given approval to the final version of the manuscript.

Conflicts of interest

There are no conflicts to declare.

Data availability

All data supporting the findings of this study are available within the article and its supplementary information (SI) files.

Supplementary information: the SI contains additional solid-state ^{13}C and ^{31}P MAS NMR spectra, N$_2$ adsorption–desorption isotherms, thermogravimetric analyses (TGA), FT-IR spectra, and XRD patterns of N-AS, P-AS, N-C and P-C. See DOI: https://doi.org/10.1039/d5cy01271f.

Acknowledgements

Notes and references

1 S. T. Wilson, B. M. Lok and E. M. Flanigen, *US Pat.*, 4310440, 1982.
2 S. T. Wilson, B. M. Lok, C. A. Messina, T. R. Cannan and E. M. Flanigen, *J. Am. Chem. Soc.*, 1982, **104**, 1146–1147.
3 H. Hussein, A. Vivian, L. Fusaro, M. Devillers and C. Aprile, *ChemCatChem*, 2020, **12**, 5966–5976.
4 K. Tawbi, A. Simon-Masseron and J. Patarin, *Microporous Mesoporous Mater.*, 2013, **169**, 192–200.
5 L. Li, F. Pan, P. A. Tanner and K. L. Wong, *ACS Appl. Nano Mater.*, 2020, **3**, 1961–1971.
6 B. Qiu, W. D. Lu, X. Q. Gao, J. Sheng, M. Ji, D. Wang and A. H. Lu, *J. Catal.*, 2023, **417**, 14–21.
7 G. M. Wang, J. H. Li, C. L. Gao, J. C. Zhang, X. Zhang, Z. Z. Bao and J. H. Lin, *Solid State Sci.*, 2015, **39**, 1–5.
8 International Zeolite Association, Database of Zeolite Structures, available at: https://www.iza-structure.org/databases/.
9 I. I. de Souza Guida, E. S. M. Cutrim, A. Cabral, A. S. Aquino, K. Bernardo-Gusmão, A. C. Alcântara and A. Rojas, *Microporous Mesoporous Mater.*, 2025, **385**, 113479.
10 B. Onida, Z. Gabelica, J. Lourenco and E. Garrone, *J. Phys. Chem.*, 1996, **100**, 11072–11079.
11 W. Shen, X. Li, Y. Wei, P. Tian, F. Deng, X. Han and X. Bao, *Microporous Mesoporous Mater.*, 2012, **158**, 19–25.
12 G. Sastre, D. W. Lewis and C. R. A. Catlow, *J. Phys. Chem. B*, 1997, **101**, 5249–5262.
13 G. Sastre and D. W. Lewis, *J. Chem. Soc., Faraday Trans.*, 1998, **94**, 3049–3058.

14 L. Gómez-Hortigüela, C. Márquez-Álvarez, M. Grande-Casas, R. García and J. Pérez-Pariente, *Microporous Mesoporous Mater.*, 2009, **121**, 129–137.

15 G. V. Echevsky, Q. Weixing, A. V. Toktarev and W. Wei, *Pet. Chem.*, 2016, **56**, 244–252.

16 J. Tan, Z. Liu, X. Bao, X. Liu, X. Han, C. He and R. Zhai, *Microporous Mesoporous Mater.*, 2002, **53**, 97–108.

17 Q. Wang, W. Zhang, X. Ma, Y. Liu, L. Zhang, J. Zheng and R. Li, *Fuel*, 2023, **331**, 125935.

18 Y. Liu, W. Qu, W. Chang, S. Pan, Z. Tian, X. Meng and F. S. Xiao, *J. Colloid Interface Sci.*, 2014, **418**, 193–199.

19 H. Yang, Z. Liu, H. Gao and Z. Xie, *J. Mater. Chem.*, 2010, **20**, 3227–3231.

20 F. Schmidt, S. Paasch, E. Brunner and S. Kaskel, *Microporous Mesoporous Mater.*, 2012, **164**, 214–221.

21 X. Zhou, Z. Chen, Z. Guo, H. Yang, J. Shao, X. Zhang and S. Zhang, *J. Hazard. Mater.*, 2021, **405**, 124177.

22 M. Jabłońska, *Mol. Catal.*, 2022, **518**, 112111.

23 S. Lin, H. Li, P. Tian, Y. Wei, M. Ye and Z. Liu, *J. Am. Chem. Soc.*, 2025, **147**, 11585–11607.

24 J. Zhong, J. Han, Y. Wei and Z. Liu, *J. Catal.*, 2021, **396**, 23–31.

25 M. Yang, D. Fan, Y. Wei, P. Tian and Z. Liu, *Adv. Mater.*, 2019, **31**, 1902181.

26 T. Liu, Z. Liu, S. Jiang, P. Peng, Z. Liu, A. D. Chowdhury and G. Liu, *Chem. Soc. Rev.*, 2025, **54**, 2726–2761.

27 Y. Yang, C. Sun, J. Du, Y. Yue, W. Hua, C. Zhang and H. Xu, *Catal. Commun.*, 2012, **24**, 44–47.

28 Q. Zhu, J. N. Kondo, T. Setoyama, M. Yamaguchi, K. Domen and T. Tatsumi, *Chem. Commun.*, 2008, **41**, 5164–5166.

29 B. Gao, M. Yang, Y. Qiao, J. Li, X. Xiang, P. Wu and Z. Liu, *Catal. Sci. Technol.*, 2016, **6**, 7569–7578.

30 J. Yao, H. Tian, F. Zha, S. Ma, X. Tang, Y. Chang and X. Guo, *New J. Chem.*, 2021, **45**, 11812–11822.

31 M. Ghavipour, A. S. Mehr, Y. Wang, R. M. Behbahani, S. Hajimirzaee and K. Bahrami, *RSC Adv.*, 2016, **6**, 17583–17594.

32 R. L. Smith, S. Svelle, P. Del Campo, T. Fuglerud, B. Arstad, A. Lind and M. W. Anderson, *Appl. Catal., A*, 2015, **505**, 1–7.

33 J. Chen, J. M. Thomas, P. A. Wright and R. P. Townsend, *Catal. Lett.*, 1994, **28**, 241–248.

34 J. Chen, P. A. Wright, J. M. Thomas, S. Natarajan, L. Marchese, S. M. Bradley and P. L. Gai-Boyes, *J. Phys. Chem.*, 1994, **98**, 10216–10224.

35 Y. Hirota, M. Yamada, Y. Uchida, Y. Sakamoto, T. Yokoi and N. Nishiyama, *Microporous Mesoporous Mater.*, 2016, **232**, 65–69.

36 T. Yu, D. Fan, T. Hao, J. Wang, M. Shen and W. Li, *Chem. Eng. J.*, 2014, **243**, 159–168.

37 T. Álvaro-Muñoz, C. Márquez-Álvarez and E. Sastre, *Catal. Today*, 2012, **179**, 27–34.

38 A. Izadbakhsh, F. Farhadi, F. Khorasheh, S. Sahebdelfar, M. Asadi and Z. F. Yan, *Microporous Mesoporous Mater.*, 2009, **126**, 1–7.

39 M. Li, Y. Wang, L. Bai, N. Chang, G. Nan, D. Hu and W. Wei, *Appl. Catal., A*, 2017, **531**, 203–211.

40 L. Ye, F. Cao, W. Ying, D. Fang and Q. Sun, *J. Porous Mater.*, 2011, **18**, 225–232.

41 G. Liu, T. Peng and Z. Liu, *Chin. J. Catal.*, 2012, **33**, 174–182.

42 L. Pace, E. Dib, D. Honorato-Piva, V. Ruaux, A. Vicente and S. Mintova, *Inorg. Chem. Front.*, 2024, **11**, 6178–6189.

43 E. Dib, L. Pace, V. Sarou-Kanian, F. Dalena, D. Honorato-Piva and S. Mintova, *Microporous Mesoporous Mater.*, 2025, **381**, 113339.

44 Y. Kubota, M. M. Helmkamp, S. I. Zones and M. E. Davis, *Microporous Mater.*, 1996, **6**, 213–229.

45 B. H. Toby and R. B. Von Dreele, *J. Appl. Crystallogr.*, 2013, **46**, 544–549.

46 ImageJ, available at: https://imagej.net/ij/.

47 R. Bardestani, G. S. Patience and S. Kaliaguine, *Can. J. Chem. Eng.*, 2019, **97**, 2781–2791.

48 E. Gianotti, J. C. F. P. Brito, I. Miletto and L. Marchese, *Microporous Mesoporous Mater.*, 2022, **346**, 112310.

49 Thermo Fisher Scientific, available at: https://www.thermofisher.com.

50 M. Thommes, K. Kaneko, A. V. Neimark, J. P. Olivier, F. Rodriguez-Reinoso, J. Rouquerol and K. S. Sing, *Pure Appl. Chem.*, 2015, **87**, 1051–1069.

51 E. Bourgeat-Lami, F. Di Renzo, F. Fajula, P. H. Mutin and T. Des Courieres, *J. Phys. Chem.*, 1992, **96**, 3807–3811.

52 L. Zhang, Z. X. Jiang, Y. Yu, C. S. Sun, Y. J. Wang and H. Y. Wang, *RSC Adv.*, 2015, **5**, 55825–55831.

53 DMFit software, available at: http://www.dmfit.com.

54 A. R. Bhat, R. S. Selokar, J. S. Meshram and R. S. Dongre, *J. Mater. Environ. Sci.*, 2014, **5**, 1653–1657.

55 P. Zhao, B. Boekfa, T. Nishitoba, N. Tsunoji, T. Sano, T. Yokoi and M. Ehara, *Microporous Mesoporous Mater.*, 2020, **294**, 109908.

56 I. B. Minova, N. S. Barrow, A. C. Sauerwein, A. B. Naden, D. B. Cordes, A. M. Slawin and P. A. Wright, *J. Catal.*, 2021, **395**, 425–444.

57 J. Weitkamp, M. Hunger and U. Rymsa, *Microporous Mesoporous Mater.*, 2001, **48**, 255–270.

58 I. Halasz, B. Moden, A. Petushkov, J. J. Liang and M. Agarwal, *J. Phys. Chem. C*, 2015, **119**, 24046–24055.

59 W. Jin, B. Wang, P. Tuo, C. Li, L. Li, H. Zhao, X. Gao and B. Shen, *Ind. Eng. Chem. Res.*, 2018, **57**, 4231–4236.

60 S. Akhgar, J. Towfighi and M. Hamidzadeh, *J. Mater. Res. Technol.*, 2020, **9**, 12126–12136.

61 J. Wu, R. Chu, X. Meng, B. Yang, P. Li, M. Dai and W. Li, *Ind. Eng. Chem. Res.*, 2023, **62**, 8684–8695.

62 F. Yaripour, Z. Shariatinia, S. Sahebdelfar and A. Irandoukht, *Microporous Mesoporous Mater.*, 2015, **203**, 41–53.

63 S. van Donk, A. H. Janssen, J. H. Bitter and K. P. de Jong, *Catal. Rev.:Sci. Eng.*, 2003, **45**, 297–319.

64 M. Signorile, D. R. Gama, F. Bonino, S. Svelle, P. Beato and S. Bordiga, *Catal. Today*, 2019, **336**, 203–209.

65 D. S. Wragg, D. Akporiaye and H. Fjellvåg, *J. Catal.*, 2011, **279**, 397–402.

66 B. P. Hereijgers, F. Bleken, M. H. Nilsen, S. Svelle, K. P. Lillerud, M. Bjørgen and S. Olsbye, *J. Catal.*, 2009, **264**, 77–87.

1410 | *Catal. Sci. Technol.*, 2026, **16**, 1400–1410

This journal is © The Royal Society of Chemistry 2026